

# Engineering surface electrostatics affords control over morphological preference, synergy, and activity in polymer degrading enzymes

**Authors:** Liliana Oliveira<sup>a</sup>, Elaine M. Rudge<sup>a</sup>, Michael Zahn<sup>b,c</sup>, Victoria Bemmer<sup>a</sup>, Kerry R. Green<sup>a</sup>, Andrew R. Pickford<sup>a</sup>, Bruce R. Lichtenstein<sup>a\*</sup>

<sup>a</sup> Centre for Enzyme Innovation, School of the Environment and Life Sciences, University of Portsmouth, UK

<sup>b</sup> Hannover Medical School, Fritz-Hartmann-Centre for Medical Research, Hanover, DE

<sup>c</sup> Martin Luther University Halle-Wittenberg, Biocenter, Core Facility Protein Production, Halle, DE

\* Corresponding author: [bruce.lichtenstein@port.ac.uk](mailto:bruce.lichtenstein@port.ac.uk)

## Abstract

The biocatalytic recycling of plastics, such as polyethylene terephthalate (PET), promises a sustainable alternative to our present open-loop cycles. Engineering of PET-hydrolases for this purpose has focused on improving activity near the glass-transition temperature of the polymer by increasing their thermostability, neglecting other features of the protein-polymer system that affect enzymatic activity. Here, we isolate the effect of electrostatics on the activity of a thermophilic PETase by rationally redesigning its surface charge, while preserving its thermodynamic properties. The enzyme variant, *S*<sup>Inv</sup>, shows orders of magnitude improvements in binding affinity and in activity towards untreated plastic films, with inverted morphological preference. When combined, the wildtype enzyme and *S*<sup>Inv</sup> act synergistically, revealing an entirely new mechanism for cooperative activities driven by complimentary electrostatic interactions at the PET surface. These findings highlight unexplored avenues in improving PETase function through the control of morphological preference or introduction of protein cooperativity by exploiting protein electrostatics.

## Introduction

Using enzymes for biocatalytic depolymerisation of plastics provides a low-energy and low-resource alternative to the current open-loop recycling of common consumer materials<sup>1</sup>. In the case of polyethylene terephthalate (PET), this process allows for the nearly quantitative recovery of the constituent monomers terephthalic acid (TPA) and ethylene glycol (EG), making new routes to (bio)-chemical valorisation and repolymerisation accessible<sup>2,3</sup>. The range of PETases, enzymes capable of carrying out this conversion, has also been expanded in recent years through discovery and further engineering<sup>4-8</sup>. Most of these research efforts have targeted large-scale bio-recycling through increases in enzymatic thermostability, allowing for improved reaction rates and depolymerisation extents by taking advantage of higher polymer chain mobility near the bulk PET glass transition temperature ( $T_g$ )<sup>9-14</sup>. This primary focus on thermostability has deepened our understanding of thermodynamically important structural features of PET-degrading enzymes<sup>10,14</sup>; however, it has left obscure much of the fundamental nature of the interactions between the proteins and the polymer surface, which ultimately governs enzymatic selectivity, optimal conditions and industrial performance.

Plastic-degrading enzymes face a multitude of challenges associated with the physical-chemical properties of their solid, hydrophobic substrate beyond polymer chain dynamics, which cannot be overcome by enhanced enzymatic thermostability and higher reaction temperatures. On solid substrates, catalytic activities can be influenced by restricted diffusion, variations in the density of surface charge, degree of crystallinity, and protein-protein interactions<sup>15-19</sup>. These complications have been shown to underlie some of the more counter intuitive behaviours we observe in natural PETases, such as diminished activities at elevated enzyme concentrations<sup>17,20,21</sup> which prevent some members of the enzyme family from being used at an industrial scale. Studying such attributes can therefore clarify fundamental enzyme-polymer interactions underlying catalytic activities, allowing us to better engineer biocatalysts towards industrial recycling applications.

In this study we examine *S*<sup>Cut</sup>, a highly active, thermostable PETase from *Saccharopolyspora flava* most closely related to PHL7<sup>8</sup> (Figure 1), previously reported<sup>4</sup> to have an exceptional preference for micronized PET powder over amorphous PET film. We sought to understand the molecular basis for this morphological preference, hoping to gain insight into how substrate specificity is controlled. Through focused structural analysis, we identified that the principal feature differentiating *S*<sup>Cut</sup> from other PETases was its markedly negative charge; to explore the implications of this property, we used a rational protein design approach that maintained the thermodynamic stability of *S*<sup>Cut</sup> while inverting its overall charge. This allowed us to clarify the role of protein electrostatics in substrate morphological preference and provided new insights into how we can use protein

51 charge to exploit protein-protein interactions at the plastic surface. By connecting structural analysis with careful  
52 protein design, this study contributes to advancing the development of more efficient targeted strategies for  
53 improving enzymes for plastic biodegradation.

## 54 Results and Discussion

### 55 Structural analysis of *SfCut* and surface charge redesign

56 To understand the parameters that influence the substrate morphological preference of *SfCut*, we carefully  
57 examined its structure. Like other reported PETases, *SfCut* (PDB: 7QJP) adopts a typical alpha-beta hydrolase  
58 fold, with a conserved disulfide bond between Cys243 and Cys260. The active site matches that of a typical PET-  
59 degrading serine hydrolase, composed of a catalytic triad (Ser132, Asp178 and His210), a conserved tryptophan  
60 (Trp157), an oxyanion hole (Phe64 and Met133) and a lipase box. Despite these features, *SfCut* is strikingly  
61 different to other highly active PETases owing to its negative surface charge and total charge density of -0.55  
62 per kDa at neutral pH. These charges are mostly found on the surface opposite to the active site, away from  
63 residues expected to directly interact with the plastic (Figure 2a/c). This pronounced charge appears to modulate  
64 the morphological selectivity of *SfCut*, causing its activity to drop considerably between pH 6.0 and pH 7.5 on  
65 films while it increases on amorphous powders<sup>4</sup>. As PET has a stable, negative zeta potential independent of pH  
66 at these conditions<sup>22</sup>, the changes in depolymerisation rates implicate the involvement of both protein and  
67 polymer electrostatics as significant factors in these properties.

68 We aimed to investigate how protein charge influences substrate morphology preference of *SfCut* by extensively  
69 redesigning its surface. To ensure clarity in our analysis, we sought to isolate the effects of charge substitutions  
70 from inadvertent changes to enzyme activity caused by variations in protein thermostability. To avoid this, we  
71 selected a manual design approach over computational methods, as the later have been constructed in a way  
72 that produces stabilised proteins as outputs. For design purposes, all charged residues in the crystallographic  
73 structure, including histidines involved in salt bridges, were identified and counted towards the overall protein  
74 charge (-16). Owing to the lack of observed crystallographic density, we did not count the first and last glutamic  
75 acid residues in the sequence.

76 To minimise disruption of the protein-polymer interface and the active site, only residues at a distance greater  
77 than 10 Å from the catalytic triad were considered for mutation. For the purposes of design, we ranked residues  
78 based on how amenable to change they might be, excluding those that were buried, involved in critical polar  
79 contacts, stabilising secondary structural elements, or providing an ambiguous structural role. Our choices of  
80 sites for mutation were supported by referencing the position-specific scoring matrix (PSSM) of *SfCut*  
81 (Supplementary Spreadsheet 1) excluding residues at highly conserved sites. As a priority for mutation, we  
82 focused on changing isolated negatively charged residues on *SfCut*'s surface, considering structural context to  
83 minimise steric clashes and preserve native contacts. Once all the free residues amenable to change were  
84 exhausted, we proceeded to consider mutations within larger salt-bridge clusters followed by neutral surface  
85 residues. In the interest of investigating solely the effect of the surface charge, we did not intentionally introduce  
86 mutations that could create new stabilising interactions.

87 The redesigned variant, here referred to as *SfInv* (*SfInv*), incorporates 24 mutations (Supplementary Table  
88 2; Supplementary Figure 2) at sites with an average information content of 0.41, resulting in an overall charge of  
89 +16 ( $\Delta_{\text{charge}}$  of +32) and a charge density of + 0.54 per kDa at neutral pH. Structural predictions using  
90 ColabFold<sup>23,24</sup> and ESMfold<sup>25</sup> (pLDDT > 0.9, Supplementary Figure 3) closely align with the crystal structure of  
91 *SfCut*, having  $C_\alpha$  RMSD values of 0.38 Å and 0.52 Å, respectively. These results suggested that the redesign was  
92 likely to preserve the protein fold, without introducing structural changes that could impact enzymatic function.

### 93 Biophysical characterisation of *SfInv*

94 We sought to confirm that the extensive surface modifications introduced to *SfInv* did not impact its biophysical  
95 properties or its ability to hydrolyse PET plastic. *SfInv* expressed in *E. coli* at comparable levels to the wildtype  
96 enzyme, and its identity was confirmed by mass spectrometry after purification (Supplementary Spreadsheet 2).  
97 Both *SfInv* and *SfCut* showed similar melting temperatures and thermo-kinetic profiles when analysed by DSC.  
98 The apparent  $T_m$  were 73 °C for *SfInv* and 76 °C for *SfCut* (Figure 2d, Supplementary Figure 4, Supplementary  
99 Table 3), with both enzymes unfolding in a single irreversible step therefore realising our design ambition of  
100 minimising the impact on thermodynamic stability.

101 The protein fold and success of the design were further confirmed through circular dichroism (CD) and structure  
102 determination by X-ray crystallography. *SfInv* readily crystallised under several conditions, and its structure was  
103 solved to a final resolution of 1.17 Å (Supplementary Table 4). The asymmetric unit in the structure contained

104 two chains, which aligned with a C<sub>α</sub> RMSD 0.24 Å, and the more complete chain B was used for structural  
105 analysis. The solved crystallographic structure of *SfInv* (PDB: 9EWR) confirmed that the enzyme retained its  
106 alpha-beta hydrolase fold (Figure 2b) and exhibited the expected positively charged surface (Figure 2c).  
107 Structural alignment with the wildtype protein yielded a C<sub>α</sub> RMSD 0.36 Å and a TM-score<sup>26</sup> of 0.99 (Figure 2b),  
108 demonstrating that the overall fold and structure were preserved, despite extensive modification. We were able  
109 to confirm that no new stabilising interactions were introduced, and that the backbone conformation, disulfide  
110 bond, and salt-bridges remained largely intact, with the only exceptions being due to crystallographic contacts  
111 spanning symmetry related monomers (Supplementary Figure 5). CD also revealed that both proteins remain  
112 well folded under the reported optimum reaction temperature of *SfCut* (50 °C) (Figure 2e).

113 With confidence in the achievement of our structural design goals, we explored the activity of *SfInv* on  
114 amorphous PET powder. *SfInv* exhibited an optimum reaction temperature at 50 °C, similar to that of the  
115 wildtype enzyme (Figure 2d), but demonstrated a higher pH optimum (pH 9) compared to *SfCut* (pH 7.5). This  
116 shift to a higher pH optimum aligns with the activity profiles of positively charged PETases, which demonstrate  
117 pH optima above pH 8<sup>4,27</sup>. We anticipated that the changes in the surface charge between *SfCut* and *SfInv* could  
118 lead to substantial differences in their binding affinity to PET. Indeed, despite its relatively high activity, *SfCut*  
119 showed no appreciable binding to the amorphous PET powder under tested conditions (Figure 3b,  
120 Supplementary Figure 6). This stands in clear contrast to *SfInv*, which demonstrated a K<sub>d</sub> of less than 4.5 nM  
121 with a surface coverage ( $\Gamma_{\max}$ ) of 10-16.5 nmol g<sup>-1</sup> PET, consistent with characteristics measured with other  
122 highly active PETases<sup>28</sup>. These results confirmed the success of our design efforts, and provided a basis for us to  
123 examine the isolated effects of protein charge on PET-degrading activities and morphological preference.

#### 124 **The role of surface charge on protein-polymer interactions**

125 To explore how their significant difference in protein surface charge manifested in terms of depolymerase activity  
126 across PET morphologies, we examined *SfCut* and *SfInv* on three PET substrates: amorphous powder (aPow),  
127 amorphous film (aFilm) and semi-crystalline powder (cPow) (Figure 3a, Supplementary Figure 7). *SfInv*  
128 demonstrated higher activity than the wildtype enzyme across all substrates tested, with broader pH and  
129 temperature optima, as well as three-fold and six-fold more product release on semi-crystalline powders and  
130 amorphous powders respectively. Our results confirmed previous observations that *SfCut* has a considerably  
131 lower activity on films compared to powders, independent of substrate crystallinity. In contrast, *SfInv* showed an  
132 inverted selectivity: its activity on films was enhanced, approximately 2-fold higher than on powders,  
133 demonstrating that enzyme specificity for different substrate morphologies is a genetically encoded, engineerable  
134 property. This corresponds to over 200-fold enhancement in the activity on amorphous PET films compared to  
135 *SfCut*, effected simply by surface charge inversion. Despite the substantial difference in evident binding affinity  
136 to amorphous powders, both enzymes show activity saturation on amorphous films above 250 nM, confirming  
137 that binding alone is insufficient to explain their catalytic properties (Supplementary Figure 8). Although not an  
138 intended outcome of our design process, *SfInv* demonstrated a similar level of conversion as the most promising  
139 industrialised enzyme, LCC<sup>ICCG</sup>,<sup>10</sup> at their respective optima (Figure 3a). In a direct comparison at 50 °C, *SfInv*  
140 outperformed LCC<sup>ICCG</sup> at laboratory scale (Supplementary Figure 9).

141 Although the greatly enhanced binding affinity observed with *SfInv* can partially explain its higher enzymatic  
142 activity, differences in enzymatic morphological preference must be caused by a change in how the differently  
143 charged enzymes interact with the polymer. Electrostatic interactions between the polymer surface and the  
144 enzymes can be mediated by both unspecific and specific interactions with ions in solution, therefore we  
145 assessed the activities of both enzymes at a range of ionic strengths, using both monovalent and divalent salts.  
146 The negatively charged wildtype enzyme, *SfCut*, showed a monotonic rise in activity on amorphous films as ionic  
147 strength increased from 0 M to 4 M, with a relative activity enhancement of nearly 600-fold (Figure 3c, &  
148 Supplementary Figure 10a). This behaviour contrasts with that of some of the best-performing PETases, such as  
149 LCC<sup>ICCG</sup>, where the depolymerase activity is not affected by the ionic strength of the solution (Figure 3c &  
150 Supplementary Figure 10b). For *SfInv* the effect of ionic strength was less pronounced (Figure 3c), with activity  
151 peaking at 250 mM ionic strength at approximately five-fold higher than in buffer with 0 M salt, before declining  
152 to approximately 7% of its maximal value at 2 M (Supplementary Figure 10a). These results on amorphous films  
153 were consistent across different salts (Supplementary Figure 10), indicating that the selectivity observed in *SfCut*  
154 and *SfInv* is driven by electrostatic interactions between the enzyme and the polymer surface, rather than by  
155 specific interactions mediated by salts.

156 Interestingly, the effect of ionic strength on the enzyme activity was distinct on amorphous powders. *SfInv*  
157 showed the same monotonic rise in activity as *SfCut*, although less pronounced (Supplementary Figure 10c), with  
158 both enzymes seeing no benefit to activity above an ionic strength of 1 M. Overall, positively charged *SfInv* sees  
159 relatively moderate benefits of increased ionic strength, with a greater effect observed on powders than films,

160 whereas *SfCut* shows substantial improvements in activity with salt, benefitting more on films than powders. This  
161 demonstrates that the interplay between the electrostatic fields of the polymer and the protein varies between  
162 polymer morphologies, influencing the observed selectivity of the two enzymes, with notably more dominant  
163 effects on PET film digestions.

164 Despite the benefit of ionic strength on the activity of *SfCut*, it is important to note that the total product  
165 released by *SfCut* did not surpass that of *SfInv* at its maximum under the conditions tested. Additionally, while  
166 increased salt concentration did have an effect on the apparent  $T_m$  of *SfCut*, causing an increase of 4 °C at 2 M  
167 sodium chloride, no such change was observed for *SfInv* (Supplementary Figure 11). This suggests that some of  
168 the activity improvement in *SfCut* with increasing ionic strength may be a result of enhanced thermostability, an  
169 effect that is absent in *SfInv*.

#### 170 ***SfInv* shows greatly enhanced PET-degrading activity at pilot scale and on post-consumer waste**

171 The improved selectivity of *SfInv* towards amorphous PET films under analytical conditions suggested a potential  
172 for digesting unmodified amorphous films at pilot scale, pH-controlled experiments. Under these conditions (1  
173 mg<sub>enzyme</sub> g<sub>PET</sub><sup>-1</sup> with high solids loading of 20% w/v)<sup>1,29</sup>, the wildtype enzyme (*SfCut*) demonstrates limited  
174 activity, achieving less than 1% substrate conversion and a monomeric product yield of 0.15 g/L as measured by  
175 HPLC. In contrast, the engineered *SfInv* exhibited significantly higher efficiency, achieving approximately 8%  
176 substrate conversion within 24 hours (Figure 4a), with a monomer yield of 18.6 g/L. Strikingly, at substantially  
177 lower enzyme loading (1 μM, ~0.15 mg<sub>enzyme</sub> g<sub>PET</sub><sup>-1</sup>), *SfInv* achieved the same high levels of conversion within the  
178 same time frame, suggesting there is substantial potential for reaction condition optimisation to maximise the  
179 digestion of amorphous PET films while reducing resource requirements (Supplementary Figure 12).

180 Comparable results were also found to be true on untreated post-consumer waste (PCW) in the form of PET-film  
181 sandwich trays (Figure 4b, Supplementary Table 5, Supplementary Figures 13 and 14). *SfInv* efficiently digested  
182 over 10% of the waste within 24 hours, achieving a measured yield of 19.25 g/L, while *SfCut* yielded negligible  
183 amounts of product (Figure 4b). This further highlights that it may be possible to engineer enzymes specifically  
184 targeting the processing of complex post-consumer waste streams of PET with limited pre-treatments, upstream  
185 of current methods reliant on resource-intensive preparation of micronized powders.<sup>29</sup>

#### 186 ***SfCut* and *SfInv* act synergistically in degrading aPET films**

187 Building on the evident enhancement in activity and change in selectivity of *SfInv* over *SfCut* on PET substrates,  
188 we sought to understand whether the enzymes act at distinct sites on the PET surfaces with differing geometries  
189 or electrostatic charge, which could account for the observed differences in morphological preferences and allow  
190 for the enzymes to work synergistically in degrading PET. Specifically, we hypothesised that the amount of  
191 product released from a mixture of the two enzymes could exceed the sum of the product release for each  
192 enzyme individually at its respective concentration. To quantify this, we define synergy as:

193 (1) 
$$\text{Synergy} \equiv \frac{\text{PR}_{\text{mix}}}{\text{PR}_{\text{SfCut}} + \text{PR}_{\text{SfInv}}} > 1$$

194 where PR<sub>*SfCut*</sub>, PR<sub>*SfInv*</sub>, and PR<sub>mix</sub> are the product released by each enzyme at specified concentrations, and their  
195 mixture, respectively. When *SfCut* and *SfInv* were mixed at different concentrations and ratios, and applied to  
196 PET films, we observed clear evidence of synergistic activity (Figure 5a). The effect is most notable at lower  
197 concentrations of *SfInv*, with a synergy value above 2 (Figure 5c). However, at elevated concentrations of *SfInv*,  
198 the synergistic benefit is lost, possibly owing to surface crowding<sup>17,20</sup> or competition for binding sites on the  
199 plastic substrate. In contrast, increasing *SfCut* does not eliminate the observed synergy, suggesting that each  
200 enzyme plays a distinct role when acting in concert on the film surface.

201 To further clarify the mechanism of the synergistic activity, we explored potential causes involving the differing  
202 enzyme charges. One possibility was that the enzymes might assemble in solution in a way that enhances their  
203 stability and activity. To test this, we incubated the enzymes together at elevated concentrations (~ 34 μM,  
204 compared to the 0.05-1 μM enzyme concentrations used in polymer digestions) and evaluated whether they form  
205 complexes by size exclusion chromatography on the mixture (Figure 5e); no shift was observed in the elution  
206 profile, suggesting that the enzymes do not appreciably bind to each other in solution. To exclude the possibility  
207 that the enzymes are targeting different sites on the polymer chain and therefore modifying the plastic surface  
208 such that it becomes a better substrate for the oppositely charged enzyme, we examined whether the enzymes  
209 showed a stepwise synergy. The activities of the enzymes were evaluated on amorphous PET film coupons that  
210 had been pre-treated with either *SfCut* or *SfInv* (Figure 5d), with no significant difference in activity observed on  
211 films pre-treated with either enzyme, showing that the surface targets for both enzymes are largely the same.

212 Given these findings, and that *S/Cut* alone shows negligible binding to PET, it is likely that the synergy observed  
213 at principally low concentrations of *S/Inv* is a result of charge masking, similar to that of the ionic strength  
214 experiments. In this case, *S/Inv* binds to the plastic surface masking the negative charges of the polymer and  
215 any bound *S/Cut*, which in turn allows more *S/Cut* to bind productively. Similar effects have been previously  
216 observed with the use of synthetic surfactants<sup>30</sup>, where anionic detergents were used to increase the negative  
217 surface charge of the polymer, therefore attracting the cationic *IspETase*<sup>31</sup> to the surface, accelerating enzymatic  
218 degradation. In this case, however, the enzymes themselves are modulating the surface charge.

219 The difference in how the film surface is modified by the enzymes acting individually or as a mixture can be  
220 visualised after partial digestion of PET coupons using SEM (Figure 5b). *S/Cut* increases the roughness of the  
221 surface leaving what appears to be thread-like crystalline regions behind, whilst *S/Inv* shows broad pitting, a  
222 surface modification commonly observed with other highly active PETases<sup>18,31</sup>. However, with the enzyme  
223 mixture, an unusual double-pitting effect is observed. Broad pits similar in dimensions to those formed by *S/Inv*  
224 contain deeper pits within them, perhaps from *S/Cut* being ‘funnelled’ into the centre of areas where the  
225 positively charged *S/Inv* masks the negative charge on the surface of the film.

226 As far as we are aware, this is the first time that synergy has been observed in enzymes directly modifying  
227 plastic surfaces. These results reveal a previously unexplored mechanism by which enzyme mixtures can  
228 enhance the degradation of plastic through beneficial electrostatic interactions, offering new opportunities for  
229 improving bio-recycling through synergistic enzymatic activity.

## 230 **Conclusions**

231 Prior to this study the most significant changes in the activity of PET degrading enzymes were realised by  
232 increasing the performance of the biocatalysts at elevated temperatures, where the polymer is more dynamic.  
233 This focus on thermostability has obfuscated how other physical-chemical properties of the polymer surface  
234 influence the activity of PETases, limiting our understanding on the enzyme-substrate interactions at play.

235 Here, by rational redesign of the surface of a highly active PETase, *S/Cut*, we were able to investigate the impact  
236 of electrostatics on enzymatic activity in the absence of confounding factors like thermodynamic stability or  
237 changes in features near the active site<sup>13,30,32</sup>. Through carefully crafted studies on the effects of ionic strength  
238 on product released from different substrates, we demonstrate that substrate selectivity is driven by polymer  
239 morphologies having distinct electrostatic profiles, and therefore influencing enzyme-surface interactions in  
240 contrasting manners. Measured zeta potentials are known to have smaller magnitudes on rough surfaces than on  
241 smooth surfaces<sup>33,34</sup>, and the impacts of this are likely manifesting here. Within the diffuse layer around the  
242 negatively charged polymer surface, the anionic *S/Cut* experiences repulsion while the cationic *S/Inv* experiences  
243 attraction, with these interactions being more pronounced on smooth films than on rough powders.

244 By focusing on electrostatic interactions governing the activity of PET degrading enzymes at the polymer surface,  
245 we demonstrated that it is possible to not only tune the selectivity of PETases for substrates of differing  
246 morphologies, but also increase their binding affinity through the rational engineering of surface charge away  
247 from the active site. The process of introducing large scale changes in protein surface electrostatic potential in  
248 *S/Inv* also afforded substantially improved activities on all PET substrates tested, exposing the benefits of using  
249 an electrostatically-oriented approach to engineering plastic depolymerases for improved activities at the low salt  
250 concentrations relevant for industrial processes. As we demonstrate through the preservation of the  
251 thermodynamic stability of *S/Inv*, this approach is complementary to established methods designed to enhance  
252 the thermostability of enzymes and can be introduced in the engineering process towards better industrial PET  
253 depolymerases.

254 We also found that synergistic activity between PETases can be realised through the applications of  
255 complementarily charged proteins. While the enhancement in activity we observed on films is relatively modest,  
256 just over two-fold, this advance is the first method for building synergy into enzymes acting at plastic surfaces  
257 and opens the door to engineering campaigns specifically tailored towards improving it. In contrast to synergies  
258 between enzyme pairs acting at different chemical sites on a substrate, the mechanism of synergy in this case  
259 appears to depend upon the electrostatic masking effect of the positively charged *S/Inv* when bound to PET,  
260 which in turn promotes the activity of the negatively charged *S/Cut*. This mechanism is likely generalisable and  
261 opens the possibility of exploiting this discovery to reduce the enzyme loading needed for industrial processes or  
262 to create dynamic mixtures of enzymes capable of accommodating variations in surface electrostatics across  
263 substrates or over the course of depolymerisations.

264 Through isolating the effect of electrostatics on *SfCut*'s activity on PET, we have been able to establish an  
265 engineering approach that allows tuning of binding affinity, improvement of enzymatic turnover, control of  
266 substrate morphological preference, and introduction of functional synergy in PETases. These insights not only  
267 expand the repertoire of established features under the control of rational protein design for plastic  
268 depolymerases, but are also likely not limited to PET. As such, we expect these results to be translatable to  
269 enzymes capable of digesting a broad range of synthetic polymers, and that the considerations established here  
270 will prove crucial when finding and engineering enzymes to tackle plastics found in complex industrial and post-  
271 consumer waste streams.

## 272 Materials and Methods

273 Amorphous PET film (ES30-FM-000145) and semi-crystalline PET powder (ES30-PD-006031) were purchased  
274 from Goodfellow. Post-consumer plastic waste was obtained from PET sandwich packaging. All reagents for  
275 molecular biology and strains were purchased from New England Biolabs. All other reagents and buffer  
276 components were acquired from Fisher Scientific or Merck, unless stated otherwise.

277 **Phylogenetic and sequence analysis:** Protein sequences of reported PETases were aligned using  
278 ClustalOmega<sup>35</sup> with default settings. A phylogenetic tree was built from the sequence alignment using IQtree<sup>36</sup>  
279 with 100,000 UltraFast bootstraps<sup>37</sup>, nearest neighbour interchange (NNI) search, automatic model selection<sup>38</sup>,  
280 and 100,000 cycles of single branch testing (SH-aLRT)<sup>39</sup>. Sequence identities were found using protein BLAST<sup>40</sup>  
281 with default settings. The position specific scoring matrix was calculated in POSSUM<sup>41</sup> using Uniref50 as the  
282 database, with 3 iterations and an E-value threshold of 0.001.

283 **Manual surface redesign:** The surface redesign was done manually using the crystal structure of *SfCut* (611,  
284 PDB: 7QJP). All charged residues with crystallographic densities were identified, including histidines involved in  
285 salt bridges or catalytic contacts; those that were not interacting were counted as non-charged. Redesign  
286 focused on charged surface residues more than 10 Å away from the active site not involved in any polar or  
287 evident structural contacts, when these were exhausted mutations within larger salt-bridges and to uninvolved  
288 surface neutral residues were considered. No mutations were added to purposefully increase or impair enzymatic  
289 stability and activity. The overall charge was changed from -16 to +16, by mutating negatively charged as well  
290 as neutral surface residues mostly not involved in stabilisation of the protein structure by visual inspection. The  
291 final *SfInv* sequence was modelled using ColabFold/AlphaFold2<sup>23,24</sup> and ESMFold<sup>25</sup> to confirm that no disruption  
292 to the protein structure by the design was predicted.

293 **Plasmid construction:** Genes for *SfCut* and *SfInv* were synthesised by Twist Bioscience. *SfCut* was cloned by  
294 Twist directly into pET21b(+), *SfInv* was synthesised as a gene fragment and cloned into pET28b(+) using  
295 Gibson assembly. The assembly mixture was transformed into NEB5α competent cells, DNA purified (Qiagen  
296 miniprep kit), and sequence confirmed by Sanger sequencing (Eurofins Genomics). Both constructs include a C-  
297 terminal His-tag, and were sequence optimised for *Escherichia coli*.

298 **Protein expression and purification:** Proteins were expressed using BL21(DE3) *E. coli* strain. Cells were  
299 grown in terrific broth with the selection antibiotic at 37 °C, in 4.5 L cultures in bioreactors (Eppendorf BioFlo  
300 120w) with pH and air flow control (Biocommand Bioprocessing Software). Protein expression was induced at an  
301 OD<sub>600</sub> of 1.2 for 18 hours at 20 °C, using a final concentration of 1 mM IPTG. Harvested cells were resuspended  
302 in HisTrap binding buffer (20 mM Tris-HCl pH 8.0, 300 mM sodium chloride, 40 mM imidazole) with nuclease  
303 (expressed in house) and 25mM of magnesium added. The resuspended cells were then homogenised, sonicated  
304 (Amplitude 40, 3 sec ON, 9 sec OFF for a total processing time of 6-10mins), and clarified by centrifugation at  
305 55,000 x g. Clarified lysate was filtered through a 0.45 µm MCE filter and purified by affinity chromatography on  
306 a HisTrap FF (5 mL) column, eluted over a gradient up to 500 mM imidazole. The protein peak was further  
307 purified by size exclusion chromatography using a Superdex 16/600 HiLoad 75pg equilibrated with 50 mM  
308 sodium phosphate pH 7.5, and 100 mM sodium chloride. SDS-PAGE was run to assess purity.

309 **Differential scanning calorimetry:** Apparent melting temperature ( $T_m$ ) values for the purified proteins were  
310 determined using a MicroCal PEAQ-DSC with automated sampler (Malvern Panalytical), using a buffer matched to  
311 that of the size exclusion chromatography step as reference. The analyses were performed using 1 mg/mL of  
312 protein, at a temperature range of 30-100 °C, using low feedback, at 192 °C/ hour, 96 °C/ hour, 90 °C/ hour, 48  
313 °C/ hour, 24 °C/ hour, 12 °C/ hour and 6 °C/ hour. Baseline subtraction was performed using the instrument's  
314 data analysis software. Calfitter 2.0<sup>42</sup> was used to derive the activation energy ( $E_{act}$ ), the heat capacity change  
315 ( $\Delta C_p$ ), the activation enthalpy change ( $\Delta H^\ddagger$ ), and the reference temperature of the irreversible melting step ( $T_{act}$ )  
316 using the thermal denaturation model with the lowest SSR value.

317 **Structure determination by X-ray crystallography:** *SfInv* was concentrated to 10 mg/mL and crystallised  
318 by the sitting drop vapour diffusion method using a Mosquito crystallisation robot (SPT Labtech) and SWISSCI 3-  
319 lens low profile plates in condition C8 of the SaltRx screen (Hampton Research): 0.1 M Tris pH 8.5 and 3.5 M  
320 sodium formate. Crystals were cryo-protected with 20% glycerol before flash-freezing in liquid nitrogen.  
321 Diffraction data were collected at the Diamond Light Source (Didcot, UK) at beamline I03 and automatically  
322 processed with the AutoPROC+STARANISO<sup>43,44</sup> pipeline on ISPyB. The structure was solved by molecular  
323 replacement on CCP4 Cloud using Molrep<sup>45</sup> and an AlphaFold2-model<sup>23</sup>. Coot was used for model building,  
324 followed by model refinement using Refmac<sup>46</sup>. The final structure was evaluated with MolProbity<sup>47</sup>, and the  
325 structure has been visualised in VMD<sup>48</sup> and ChimeraX<sup>49</sup>. The structure was deposited in the PDB with code 9EWR.  
326 Data and refinement statistics can be found in Supplementary Table 4.

327 **Structural characterisation by circular dichroism:** Spectra were collected on a PiStar-180 (Applied  
328 Photophysics) with water bath temperature control. Protein samples were analysed at a concentration of 0.1  
329 mg/mL in 10 mM sodium phosphate pH 7.5 with 20 mM sodium chloride at 50 °C, in a 1 mm stoppered quartz  
330 cuvette. Data collected at wavelengths between 200 and 260 nm, with half bandwidth of 1.5 nm and a  
331 wavelength interval of 0.5 nm (1 sec per point, 5 repeats), were averaged and baseline subtracted using a  
332 matched buffer blank. Raw ellipticity data was converted to mean residue ellipticity by dividing by the path  
333 length, concentration, molecular weight and number of residues.

344 **Amorphous PET powder production and analysis:** Sheets of amorphous PET film were cut into strips,  
345 immersed in liquid nitrogen and cryo-milled at 2,400 rpm in a SM300 cutting mill (Retsch), with a bottom sieve  
346 with 4 mm square holes. Subsequently, this product was reduced in size further by immersing in liquid nitrogen  
347 and cryo-milling at 18,000 rpm in a ZM200 centrifugal mill, with a 0.12 mm ring sieve with trapezoidal holes. The  
348 particle size and crystallinity of the cryo-milled amorphous PET powder was compared to that of the purchased  
349 semi-crystalline PET powder, as well as the PET film, using a CAMSIZER X2 (Microtrac MRB) and Differential  
350 Scanning Calorimetry (Supplementary Table 5, Supplementary Figures 13 and 15).

341 **Reaction quenching and product quantification by HPLC:** All reactions were quenched by addition of  
342 equal volume of HPLC-grade methanol, and PET solids removed. Samples were centrifuged at 10,000 x g, using  
343 a table-top centrifuge, prior to analyte quantification by HPLC. For samples with subsequent polymer analysis,  
344 the PET was washed by rinsing three times with a 1% (w/v) SDS solution, followed by multiple rinses with  
345 distilled water. The partially digested polymer substrates were then dried at room temperature under vacuum  
346 before analysis. The HPLC analysis was adapted from a reported UPLC method<sup>14</sup> to allow for HPLC pressures as  
347 previously described<sup>50</sup>. Samples were evaluated on a pre-equilibrated C18 Kinetex LC column (00B-4605-AN)  
348 with a guard, at 1.1 mL min<sup>-1</sup> with 0.1% formic acid and acetonitrile as the stationary and mobile phases  
349 respectively. Samples were prepared with a known dilution to an absorbance at 240 nm of around 1.0 before 10  
350 µL were loaded onto the column using an automatic sampler (Agilent). Samples were eluted with an isocratic  
351 elution at 13% mobile phase for 0.87 minutes, followed by a step to 95% mobile phase for 1.12 minutes and a  
352 re-equilibration at 13% mobile phase until a total time of 3.6 minutes. Peaks were integrated using Agilent's  
353 OpenLab software and the product quantification was performed against calibration curves of known standards  
354 (TPA, MHET, BHET). An example of the HPLC trace and elution times is provided in Supplementary Figure 16.

355 **PET degradation assays at small scale:** Unless stated otherwise, small scale assays were set up in 1.5 mL  
356 tubes with 11 mg of PET substrate, and incubated in triplicate 500 µL reactions for 24 hours at 300 rpm on  
357 thermomixers. A final concentration of 100 nM enzyme and 100 mM sodium chloride was used, in 50 mM sodium  
358 phosphate pH 7.5, or 50 mM glycine pH 9.0 for *SCut* and *SfInv* respectively. In the case of the ionic strength  
359 tests 50 mM HEPES pH 7.5 and 50 mM CHES pH 9.0 were used instead, with varying amounts of sodium  
360 chloride, magnesium chloride and sodium sulphate. These buffers were chosen in order to minimise their  
361 contribution towards the ionic strength. Nevertheless, the buffer component was fully accounted for in the ionic  
362 strength calculations by considering their pKas, and calculating the concentration and charges of their respective  
363 ionic species. The ionic strength of the solution was calculated by using the formula  $I = \frac{1}{2} n \sum_i (C_i Z_i)$ , where  $I$   
364 represents the ionic strength,  $n$  is the number of ions in solution,  $C_i$  is the concentration of a specific ion in moles  
365 per litre, and  $Z_i$  the valence of the particular ion species. For the temperature and pH optima experiments, the  
366 reactions were performed at three temperatures (40 °C, 50 °C and 60 °C) and using three different buffers (50  
367 mM MES pH 6.0, 50 mM sodium phosphate pH 7.5, and 50 mM glycine pH 9.0) with 100 mM sodium chloride. To  
368 determine the concentration dependency for each of the enzymes, both were tested individually, and together at  
369 equimolar ratios, to a final enzyme concentration ranging from 0 - 1 µM.

370 **Binding isotherms:** Binding affinities to the plastic were measured in two ways as described previously<sup>28</sup>. All  
371 samples were incubated for 1 hour at 4 °C with rolling in low-binding 1.5 mL microcentrifuge tubes (Eppendorf)  
372 to prevent loss from non-specific binding. After centrifugation, free enzyme concentrations were determined

373 using a Micro BCA protein assay kit (Thermo Scientific) with a calibration curve derived for the respective  
374 enzyme. 150 µL samples were mixed with the Micro BCA Working Reagent as per the kit's instructions, and  
375 incubated for 1 hour at 50 °C in a covered microtiter plate mixing at 300 rpm. 200 µL samples were measured at  
376 562 nm on a plate reader. *Substrate saturation:* Amorphous PET powder at a fixed substrate loading (100 g/L for  
377 SCut or 50 g/L for SInv) was incubated with 0.05 - 1.5 µM enzyme. The substrate coverage was calculated  
378 using the equation  $\Gamma = \frac{E_{tot} - E_{free}}{L_{PET}}$ , and the  $K_d$  obtained by fitting the data to the Langmuir adsorption isotherm  
379 equation  $\Gamma = \frac{\Gamma_{max} E_{free}}{E_{free} + K_d}$ , where  $\Gamma_{max}$  is the substrate coverage at surface saturation. *Enzyme saturation:* 1 µM  
380 enzyme was incubated with substrate loads ranging from 0 – 200 g/L. The bound fraction was calculated from  
381 the difference between total and free enzyme concentrations.  $K_d$  and  $\Gamma_{max}$  were derived from fitting the data to  
382 the equation<sup>28</sup>  $\theta = \frac{1}{2} \left[ \left( 1 + \frac{K_d + \Gamma_{max} L_{PET}}{E_{tot}} \right) - \sqrt{\left( 1 + \frac{K_d + \Gamma_{max} L_{PET}}{E_{tot}} \right)^2 - 4 \left( \frac{\Gamma_{max} L_{PET}}{E_{tot}} \right)} \right]$ , where the fraction bound  $\theta =$   
383  $\frac{E_{tot} - E_{free}}{E_{tot}}$ , and  $L_{PET}$  is the experimental solids loading.

384 **PET degradation assays – pilot scale and post-consumer waste:** Duplicate reactions were undertaken in  
385 250mL MiniBio Reactors (Applikon Biotechnology) to a total reaction volume of 100 mL. Reactions were carried  
386 out at 20% (w/v) solids loading and a final enzyme concentration of 1 mg of enzyme per gram of PET. Reactions  
387 were incubated at 50 °C, stirring at 200 rpm for 24 hours. Substrates used in the reactions were amorphous PET  
388 film or washed and dried post-consumer plastic film waste, roughly cut into 1 cm x 1 cm squares. All pH probes  
389 were calibrated immediately prior to analysis, pH changes were followed and maintained by the automatic  
390 addition of 1 M (SCut) or 5 M (SInv) freshly prepared sodium hydroxide via the system pump, which was  
391 calibrated prior to the experiment. The base addition was followed as a function of time by the Lucullus® Process  
392 Information Management System software and converted to percentage hydrolysis by calculating the moles of  
393 TPA neutralised. At the end of the incubation, samples were taken and quenched as described previously using  
394 an equal volume of methanol for HPLC analysis. The PET film was recovered by filtration, rinsed thoroughly with  
395 deionised water, and allowed to dry before weighing to confirm depolymerisation extent.

396 **Polymer analysis and characterisation:** Polymer DSC was performed on a Netzsch DSC 214 Polyma,  
397 equipped with aluminium crucibles and lids. Approximately 10 mg of samples was heated from 25 to 300 °C at a  
398 rate of 10 °C per minute in a nitrogen atmosphere. Measurements were performed in triplicate, and sample  
399 crystallinity was calculated using the equation % Crystallinity =  $\frac{\Delta H_m - \Delta H_c}{\Delta H_m^\circ}$ , where  $\Delta H_m$  is the enthalpy of melting  
400 of the sample  $\Delta H_c$  is the enthalpy of crystallisation of the sample and  $\Delta H_m^\circ$  is the enthalpy of melting for a  
401 theoretical 100 % crystalline sample (taken as 140.1 Jg<sup>-1</sup>).

402 **PET degradation assays for investigating synergy:** To quantitate synergy across enzyme concentrations  
403 and ratios, amorphous PET coupons were incubated in 50 mM sodium phosphate pH 7.5, 100 mM sodium  
404 chloride, for 24 hours, with various enzyme ratios and concentrations ranging from 0 – 200 nM, as per Figure 5.  
405 To investigate whether the synergy was caused by opposite charge effects between the enzymes, size exclusion  
406 chromatography was performed with 1 mg of total enzyme (~ 34 µM) on its own or at equimolar ratio using a  
407 Superdex 75 equilibrated with 50 mM sodium phosphate pH 7.5, and 100 mM sodium chloride. For the stepwise  
408 synergy studies, a final concentration of 100 nM enzyme was used. Films were pre-treated with the selected  
409 enzyme for 24 hours, reactions quenched and the coupons washed and dried as described above. Coupons were  
410 then incubated a further 24 hours with the second selected enzyme before the reactions were quenched one  
411 final time prior to product analysis by HPLC.

412 **Scanning electron microscopy:** Samples were incubated with 100 nM of the respective enzyme for 24 hours  
413 as described above in PET degradation assays for investigating synergy. For the mixed enzyme samples, a total  
414 of 200 nM enzyme at an equimolar ratio was used instead. Samples were quenched, washed and dried as  
415 described above before analysis by SEM. PET film samples were mounted onto aluminium stubs using carbon  
416 adhesive tabs, and sputter coated with Au/Pd under argon using a Quorum Q150RES (Quorum Technologies  
417 Ltd). Samples were imaged using a MIRA3 FEG-SEM Microscope (TESCAN) operated at 3 kV.

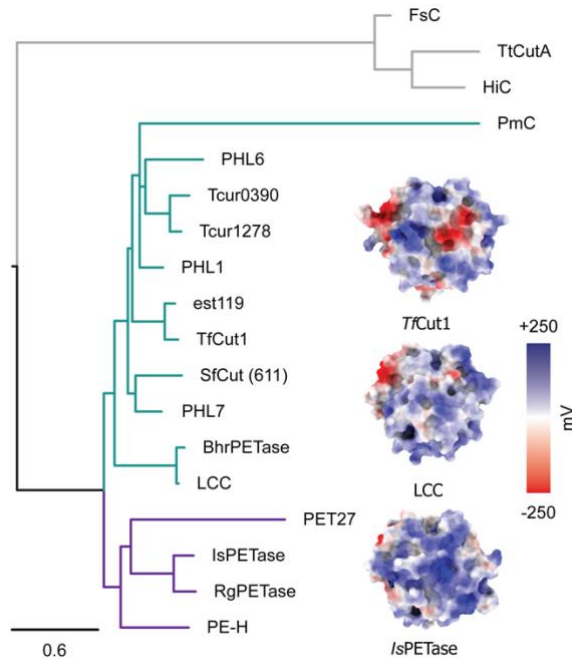
418 **Author contributions**

419 BRL conceptualised and supervised the project. The manuscript was written by LO and BRL, and reviewed by all  
420 authors. VB collected polymer DSC data. Enzymes were expressed by EMR. KRG collected crystals for structure  
421 determination of *SfInv*, and MZ solved the crystal structure. All other data was collected, processed and analysed  
422 by LO. ARP and BRL acquired funding.

423 **Acknowledgements**

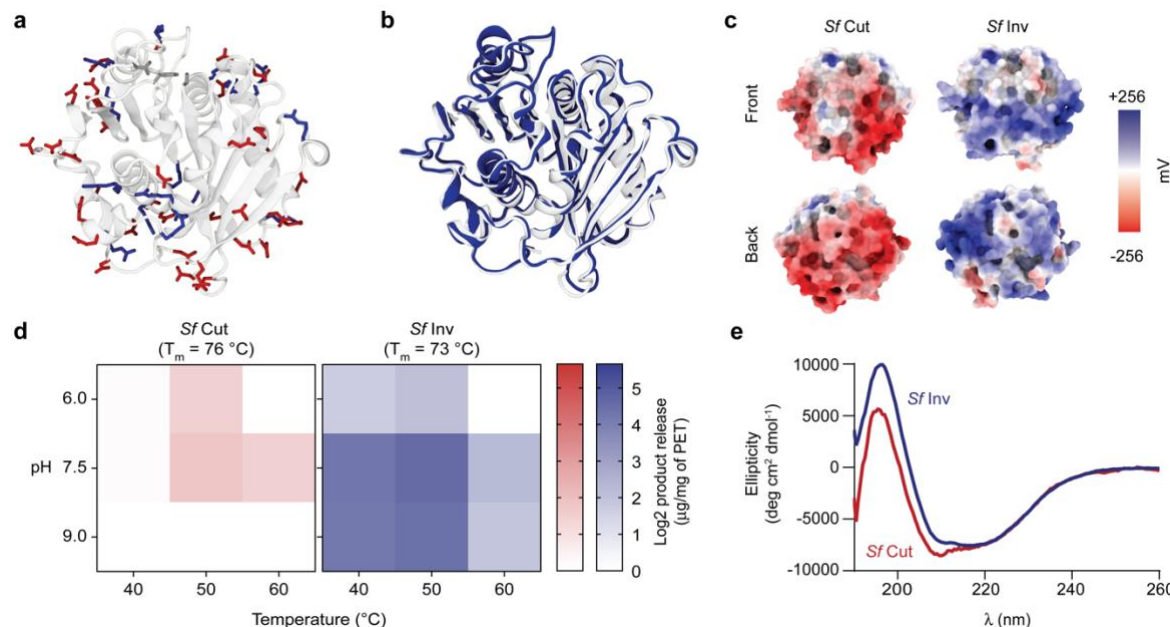
424 The authors thank Research England [E3 funding to ARP], the Royal Society [Grant RGS\R2\212336 to BRL], and  
425 the UKRI Engineering Biology Mission Hub [Grant BB/Y007972/1 to ARP, BRL and VB]. We thank Diamond Light  
426 source for beamtime [PROPOSAL MX-31440], and the staff at beamline I03 for supporting automatic data  
427 collection. We thank the Electron Microscopy and Microanalysis Unit at the University of Portsmouth, and in  
428 particular Ben Trundle, for assisting with SEM data collection. LO and BRL also thank Prof. Birte Höcker and Prof.  
429 Samuel Robson for fruitful discussions and feedback.

430 **Figures**



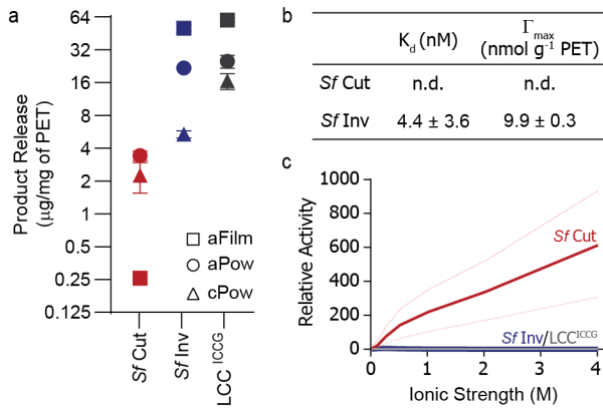
431

432 **Figure 1. Phylogenetic tree showing relationship between *S/Cut* and other previously reported PETases.** The  
433 structure of three well characterised PETases are represented as surfaces coloured by their surface potential at pH 7.5, as  
434 calculated by APBS<sup>51</sup>. *S/Cut* falls within the same clade as the thermotolerant type I PETases (green). Type II bacterial PETases  
435 are shown in purple and those of fungal origin are shown as the grey outgroup. Accession codes for the PETases used can be  
436 found in Supplementary Table 1 and the alignment used to build the tree in Supplementary Figure 1.



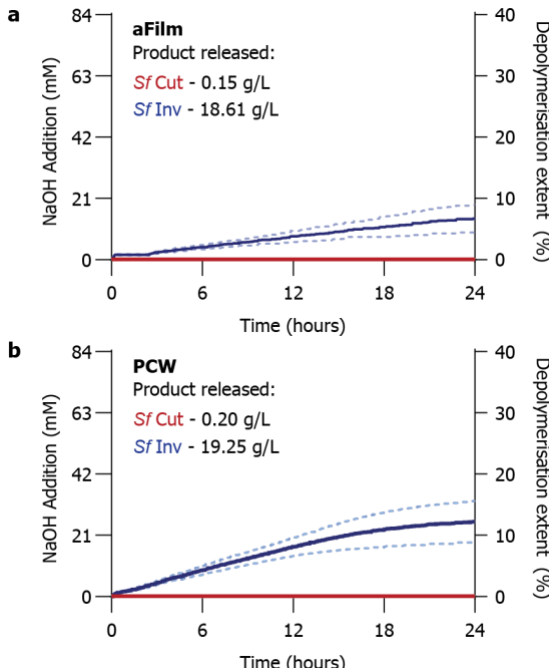
437

438 **Figure 2. Biophysical characterisation of *S/Cut* and *S/Inv*.** a Cartoon representation of *S/Cut*, with positively and negatively  
439 charged residues represented as sticks. Positive charges are shown as blue, negative charges as red. Active site residues are  
440 shown in grey at the top of the structure. b Structural alignment between *S/Cut* (white, PDB: 7QJP) and the crystal structure of  
441 *S/Inv* (blue, PDB: 9EWR) confirms the adoption of an alpha-beta hydrolase fold and the success of the design with a C<sub>α</sub> RMSD  
442 of 0.36 and a TM-score of 0.99. c Surface representation of the potential surfaces of *S/Cut* and *S/Inv* at pH 7.5, as calculated by  
443 APBS. d Heatmap for activity optima of *S/Cut* and *S/Inv* at 100 nM on amorphous PET powders across temperatures and pH.  
444 Apparent T<sub>m</sub> at a scan rate of 90 °C/hour for the respective enzymes is indicated. Additional data for PET films and semi-crystalline  
445 powders can be found in Supplementary Figure 7. e Circular dichroism spectra at 50 °C shows both enzymes remain well  
446 structured at their reaction optima.



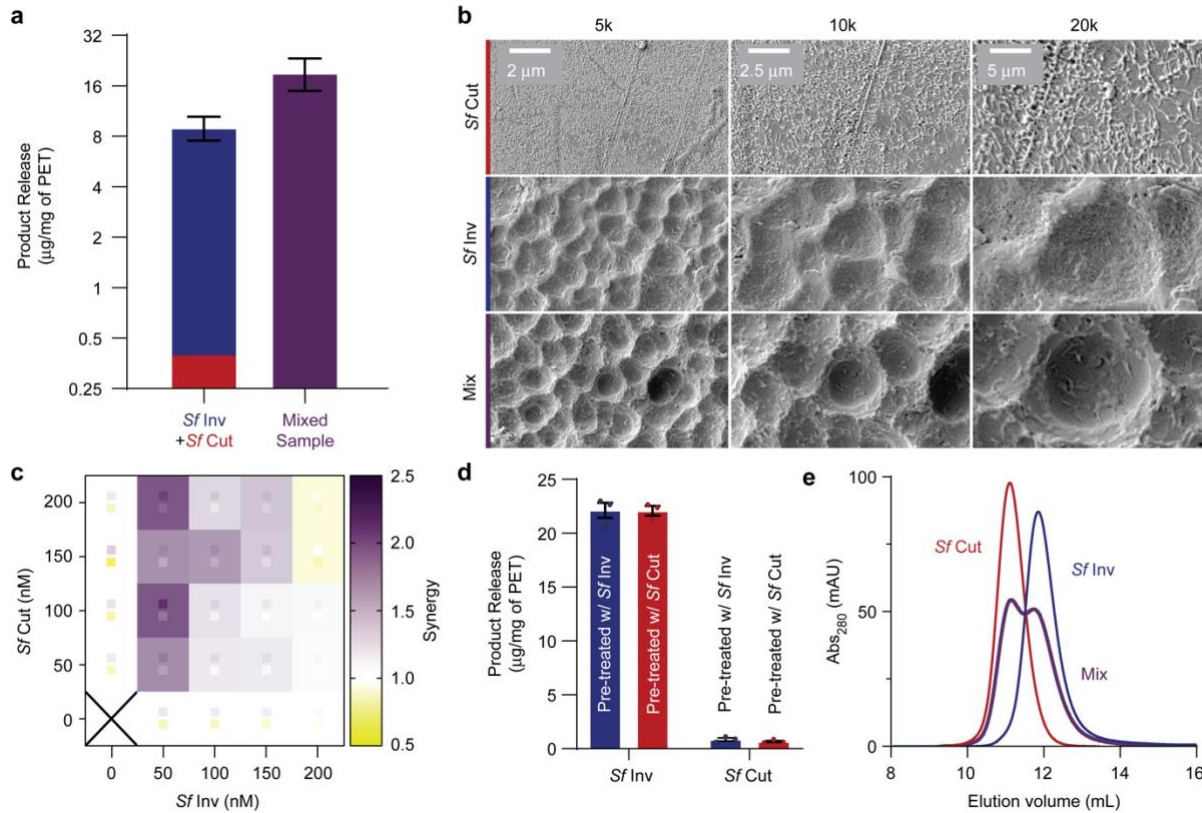
447

448 **Figure 3. Investigating how ionic strength plays a role in protein-polymer interactions.** **a** Substrate  
449 preference for *Sf*Cut, *Sf*Inv, and LCC<sup>ICCG</sup> on a Log<sub>2</sub> scale. Experiments were carried out at the optimum temperature  
450 and pH for the individual enzymes at 100 nM, with 100 mM sodium chloride. **b** *Sf*Inv has a measurable affinity to  
451 PET powders, while *Sf*Cut interacts too weakly to measure (binding curves and full statistics are detailed in  
452 Supplementary Figure 4). **c** Ionic strength affects the relative activities of *Sf*Cut and *Sf*Inv on aFilms in different  
453 ways: *Sf*Cut benefits from the increased ionic strength, whilst *Sf*Inv, like LCC<sup>ICCG</sup>, is largely not affected. Plot is  
454 shown as relative activity with respect to the activity of each enzyme in buffer without added salt. Lighter dotted  
455 lines represent standard deviations calculated with propagated error.



456

457 **Figure 4. Depolymerisation of PET at pilot scale by *Sf*Cut and *Sf*Inv.** Enzymes were incubated with 20%  
458 (w/v) PET substrate, at an enzyme loading of 1 mg per g of PET. *Sf*Cut is shown in red, whereas *Sf*Inv is shown  
459 in blue. Figure illustrates depolymerisation overtime of amorphous PET film (**a**) and post-consumer PET waste  
460 (**b**). Average trace showed as a solid line, each of the replicates are represented as dotted lines in the corresponding  
461 colour. Product release as determined by HPLC shown in each panel.



462

463 **Figure 5. Investigating the synergy between *SfCut* and *SfInv* on aPET film. a** Difference in total product  
464 release by pure enzymes and their mixture, at the condition with highest synergy (100 nM:50 nM of *SfCut* to *SfInv*).  
465 Pure enzymes are represented as a stacked plot, where red represents *SfCut* and blue *SfInv*. The enzyme mixture  
466 is represented as a purple bar. Product release is shown as a Log<sub>2</sub> scale for clarity. Error bars represent 1 SD. **b**  
467 Scanning Electron Microscopy (SEM) images of amorphous PET film after incubation with enzyme. The top two  
468 panels show the film after incubation with *SfCut* or *SfInv* individually, whilst the bottom panel shows the film after  
469 incubation with the enzyme mix. **c** Heatmap of the synergy ratios across different concentrations of *SfCut* and  
470 *SfInv*, with the purple as productive synergy and yellow as a decrease in total product release. Standard deviation  
471 is shown as smaller squares in the same colour scheme. **d** Total product release for the stepwise synergy, where  
472 the pure enzymes were incubated with an amorphous film coupon pre-digested by either *SfInv* (blue) or *SfCut*  
473 (red). Error bars represent 1 SD. **e** Chromatogram from Size Exclusion Chromatography (SEC) for *SfCut* (red),  
474 *SfInv* (blue) and a mixed sample of both enzymes at equimolar ratios (purple).

475 **References**

- 476 1. Singh, A. *et al.* Techno-economic, life-cycle, and socioeconomic impact analysis of enzymatic  
477 recycling of poly(ethylene terephthalate). *Joule* **5**, 2479–2503 (2021).
- 478 2. Gamerith, C. *et al.* Enzymatic recovery of polyester building blocks from polymer blends. *Process  
479 Biochem.* **59**, 58–64 (2017).
- 480 3. Carniel, A. *et al.* From trash to cash: current strategies for bio-upcycling of recaptured  
481 monomeric building blocks from poly(ethylene terephthalate) (PET) waste. *Green Chem.* **26**,  
482 5708–5743 (2024).
- 483 4. Erickson, E. *et al.* Sourcing thermotolerant poly(ethylene terephthalate) hydrolase scaffolds  
484 from natural diversity. *Nat. Commun.* **13**, 7850 (2022).
- 485 5. Austin, H. P. *et al.* Characterization and engineering of a plastic-degrading aromatic  
486 polyesterase. *Proc. Natl. Acad. Sci.* **115**, (2018).
- 487 6. Cui, Y. *et al.* Computational Redesign of a PETase for Plastic Biodegradation under Ambient  
488 Condition by the GRAPE Strategy. *ACS Catal.* **11**, 1340–1350 (2021).
- 489 7. Tournier, V. *et al.* Enzymes' Power for Plastics Degradation. *Chem. Rev.* **123**, 5612–5701 (2023).
- 490 8. Richter, P. K. *et al.* Structure and function of the metagenomic plastic-degrading polyester  
491 hydrolase PHL7 bound to its product. *Nat. Commun.* **14**, 1905 (2023).
- 492 9. Gao, S. *et al.* β-sheet Engineering of *IsPETase* for PET Depolymerization. *Engineering* (2024)  
493 doi:10.1016/j.eng.2024.10.015.
- 494 10. Tournier, V. *et al.* An engineered PET depolymerase to break down and recycle plastic bottles.  
495 *Nature* **580**, 216–219 (2020).
- 496 11. Shi, L. *et al.* Complete Depolymerization of PET Wastes by an Evolved PET Hydrolase from  
497 Directed Evolution. *Angew. Chem. Int. Ed.* **62**, e202218390 (2023).
- 498 12. Son, H. F. *et al.* Rational Protein Engineering of Thermo-Stable PETase from *Ideonella sakaiensis*  
499 for Highly Efficient PET Degradation. *ACS Catal.* **9**, 3519–3526 (2019).

- 500 13. Nakamura, A., Kobayashi, N., Koga, N. & Iino, R. Positive Charge Introduction on the Surface of  
501 Thermostabilized PET Hydrolase Facilitates PET Binding and Degradation. *ACS Catal.* **11**, 8550–  
502 8564 (2021).
- 503 14. Bell, E. L. *et al.* Directed evolution of an efficient and thermostable PET depolymerase. *Nat.*  
504 *Catal.* **5**, 673–681 (2022).
- 505 15. Erickson, E. *et al.* Comparative Performance of PETase as a Function of Reaction Conditions,  
506 Substrate Properties, and Product Accumulation. *ChemSusChem* **15**, e202102517 (2022).
- 507 16. Bååth, J. A., Borch, K., Jensen, K., Brask, J. & Westh, P. Comparative Biochemistry of Four  
508 Polyester (PET) Hydrolases\*\*. *ChemBioChem* **22**, 1627–1637 (2021).
- 509 17. Avilan, L. *et al.* Concentration-Dependent Inhibition of Mesophilic PETases on Poly(ethylene  
510 terephthalate) Can Be Eliminated by Enzyme Engineering. *ChemSusChem* **16**, e202202277  
511 (2023).
- 512 18. Thomsen, T. B., Hunt, C. J. & Meyer, A. S. Influence of substrate crystallinity and glass transition  
513 temperature on enzymatic degradation of polyethylene terephthalate (PET). *New Biotechnol.*  
514 **69**, 28–35 (2022).
- 515 19. Tanaka, M., Ikesaka, M., Matsuno, R. & Converse, A. O. Effect of pore size in substrate and  
516 diffusion of enzyme on hydrolysis of cellulosic materials with cellulases. *Biotechnol. Bioeng.* **32**,  
517 698–706 (1988).
- 518 20. Zhong-Johnson, E. Z. L. *et al.* Analysis of Poly(ethylene terephthalate) degradation kinetics of  
519 evolved IsPETase variants using a surface crowding model. *J. Biol. Chem.* **300**, (2024).
- 520 21. Arnling Bååth, J., Jensen, K., Borch, K., Westh, P. & Kari, J. Sabatier Principle for Rationalizing  
521 Enzymatic Hydrolysis of a Synthetic Polyester. *JACS Au* **2**, 1223–1231 (2022).
- 522 22. Pascoe, M. J., Mandal, S., Williams, O. A. & Maillard, J.-Y. Impact of material properties in  
523 determining quaternary ammonium compound adsorption and wipe product efficacy against  
524 biofilms. *J. Hosp. Infect.* **126**, 37–43 (2022).

- 525 23. Jumper, J. *et al.* Highly accurate protein structure prediction with AlphaFold. *Nature* **596**, 583–  
526 589 (2021).
- 527 24. Mirdita, M. *et al.* ColabFold: making protein folding accessible to all. *Nat. Methods* **19**, 679–682  
528 (2022).
- 529 25. Lin, Z. *et al.* Evolutionary-scale prediction of atomic-level protein structure with a language  
530 model. *Science* **379**, 1123–1130 (2023).
- 531 26. Zhang, Y. & Skolnick, J. Scoring function for automated assessment of protein structure template  
532 quality. *Proteins Struct. Funct. Bioinforma.* **57**, 702–710 (2004).
- 533 27. Arnal, G. *et al.* Assessment of Four Engineered PET Degrading Enzymes Considering Large-Scale  
534 Industrial Applications. *ACS Catal.* **13**, 13156–13166 (2023).
- 535 28. Badino, S. F., Bååth, J. A., Borch, K., Jensen, K. & Westh, P. Adsorption of enzymes with  
536 hydrolytic activity on polyethylene terephthalate. *Enzyme Microb. Technol.* **152**, 109937 (2021).
- 537 29. Uekert, T. *et al.* Life cycle assessment of enzymatic poly(ethylene terephthalate) recycling. *Green*  
538 *Chem.* **24**, 6531–6543 (2022).
- 539 30. Furukawa, M., Kawakami, N., Oda, K. & Miyamoto, K. Acceleration of Enzymatic Degradation of  
540 Poly(ethylene terephthalate) by Surface Coating with Anionic Surfactants. *ChemSusChem* **11**,  
541 4018–4025 (2018).
- 542 31. Yoshida, S. *et al.* A bacterium that degrades and assimilates poly(ethylene terephthalate).  
543 *Science* **351**, 1196–1199 (2016).
- 544 32. Ding, K. *et al.* Modulation of PETase active site flexibility and activity on morphologically distinct  
545 polyethylene terephthalate substrates by surface charge engineering. *Biochem. Eng. J.* **209**,  
546 109420 (2024).
- 547 33. Chow, R. S. & Takamura, K. Effects of surface roughness (hairiness) of latex particles on their  
548 electrokinetic potentials. *J. Colloid Interface Sci.* **125**, 226–236 (1988).

- 549 34. Duval, J. F. L., Leermakers, F. A. M. & van Leeuwen, H. P. Electrostatic Interactions between  
550 Double Layers: Influence of Surface Roughness, Regulation, and Chemical Heterogeneities.  
551 *Langmuir* **20**, 5052–5065 (2004).
- 552 35. Madeira, F. *et al.* The EMBL-EBI Job Dispatcher sequence analysis tools framework in 2024.  
553 *Nucleic Acids Res.* **52**, W521–W525 (2024).
- 554 36. Nguyen, L.-T., Schmidt, H. A., von Haeseler, A. & Minh, B. Q. IQ-TREE: A Fast and Effective  
555 Stochastic Algorithm for Estimating Maximum-Likelihood Phylogenies. *Mol. Biol. Evol.* **32**, 268–  
556 274 (2015).
- 557 37. Hoang, D. T., Chernomor, O., von Haeseler, A., Minh, B. Q. & Vinh, L. S. UFBoot2: Improving the  
558 Ultrafast Bootstrap Approximation. *Mol. Biol. Evol.* **35**, 518–522 (2018).
- 559 38. Kalyaanamoorthy, S., Minh, B. Q., Wong, T. K. F., von Haeseler, A. & Jermiin, L. S. ModelFinder:  
560 fast model selection for accurate phylogenetic estimates. *Nat. Methods* **14**, 587–589 (2017).
- 561 39. Anisimova, M., Gil, M., Dufayard, J.-F., Dessimoz, C. & Gascuel, O. Survey of Branch Support  
562 Methods Demonstrates Accuracy, Power, and Robustness of Fast Likelihood-based  
563 Approximation Schemes. *Syst. Biol.* **60**, 685–699 (2011).
- 564 40. Altschul, S. F., Gish, W., Miller, W., Myers, E. W. & Lipman, D. J. Basic local alignment search tool.  
565 *J. Mol. Biol.* **215**, 403–410 (1990).
- 566 41. Wang, J. *et al.* POSSUM: a bioinformatics toolkit for generating numerical sequence feature  
567 descriptors based on PSSM profiles. *Bioinforma. Oxf. Engl.* **33**, 2756–2758 (2017).
- 568 42. Kunka, A. *et al.* CalFitter 2.0: Leveraging the power of singular value decomposition to analyse  
569 protein thermostability. *Nucleic Acids Res.* **50**, W145–W151 (2022).
- 570 43. Vonrhein, C. *et al.* Data processing and analysis with the autoPROC toolbox. *Acta Crystallogr. D  
571 Biol. Crystallogr.* **67**, 293–302 (2011).
- 572 44. Tickle, I. J. *et al.* STARANISO. Global Phasing Ltd (2016).
- 573 45. Vagin, A. & Teplyakov, A. MOLREP: an Automated Program for Molecular Replacement. *J. Appl.  
574 Crystallogr.* **30**, 1022–1025 (1997).

- 575 46. Murshudov, G. N. *et al.* REFMAC5 for the refinement of macromolecular crystal structures. *Acta*  
576 *Crystallogr. D Biol. Crystallogr.* **67**, 355–367 (2011).
- 577 47. Williams, C. J. *et al.* MolProbity: More and better reference data for improved all-atom structure  
578 validation. *Protein Sci.* **27**, 293–315 (2018).
- 579 48. William Humphrey, Dalke, A. & Schulten, K. VMD: Visual molecular dynamics. *J. Mol. Graph.* **14**,  
580 33–38 (1996).
- 581 49. Pettersen, E. F. *et al.* UCSF ChimeraX: Structure visualization for researchers, educators, and  
582 developers. *Protein Sci.* **30**, 70–82 (2021).
- 583 50. Oliveira, L. *et al.* Investigating the effect of fusion partners on the enzymatic activity and  
584 thermodynamic stability of poly(ethylene terephthalate) degrading enzymes. *Faraday Discuss.*  
585 **252**, 468–479 (2024).
- 586 51. Jurrus, E. *et al.* Improvements to the APBS biomolecular solvation software suite. *Protein Sci.* **27**,  
587 112–128 (2018).
- 588